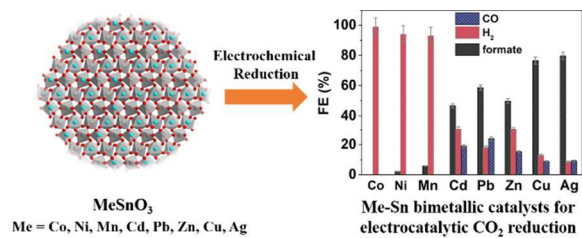


**Stannate Derived Bimetallic Nanoparticles for  
Electrocatalytic CO<sub>2</sub> Reduction**

Journal:	<i>Journal of Materials Chemistry A</i>
Manuscript ID	TA-ART-03-2018-002429
Article Type:	Paper
Date Submitted by the Author:	16-Mar-2018
Complete List of Authors:	Zhang, Xiaolong; Monash University, School of Chemistry Li, Fengwang; Monash University, School of Chemistry Zhang, Ying; Monash University, Chemistry Bond, Alan; Monash University, Chemistry Zhang, Jie; Monash University, School of Chemistry

## TOC



Stannate derived bimetallic systems can achieve highly efficient electrocatalytic CO<sub>2</sub> reduction to formate.



## Journal Name

## ARTICLE

## Stannate Derived Bimetallic Nanoparticles for Electrocatalytic CO<sub>2</sub> Reduction

Received 00th January 20xx,  
Accepted 00th January 20xx

Xiaolong Zhang,<sup>a</sup> Fengwang Li,<sup>a,b</sup> Ying Zhang,<sup>a,b</sup> Alan M. Bond<sup>a,b</sup> and Jie Zhang<sup>a,b\*</sup>

DOI: 10.1039/x0xx00000x

www.rsc.org/

The synthesis of 8 metal-Sn (metal = Mn, Co, Ni, Cu, Zn, Ag, Cd, and Pb) bimetallic materials by electrochemical reduction of their metal stannates is reported. When the metal-Sn bimetallic materials were used as electrocatalysts for electrochemical CO<sub>2</sub> reduction, bulk electrolysis results revealed that the Ag-Sn and Cu-Sn bimetallic systems showed the highest activity and selectivity for formate. When incorporated with reduced graphene oxide (rGO), their electrocatalytic performance can be further improved, making them among the best performed tin based CO<sub>2</sub> reduction electrocatalysts reported so far. The Ag-Sn/rGO catalyst reaches the highest faradaic efficiency for formate (FE<sub>formate</sub>) of 88.3% at -0.94 V vs. RHE with a current density of 21.3 mA cm<sup>-2</sup> in a 0.5 M aqueous NaHCO<sub>3</sub> solution. Comparable performance was observed from the Cu-Sn/rGO catalyst, where the highest FE<sub>formate</sub> of 87.4% and a current density of 23.6 mA cm<sup>-2</sup> were obtained at -0.99 V vs. RHE. Both catalysts exhibited high stability over a 6-hour electrolysis period with FE<sub>formate</sub> variation being less than 2%. The excellent performance of this class of bimetallic nanoparticle/rGO composite catalyst is attributed to the small size of the stannate derived bimetallic nanoparticles, the presence of a SnO<sub>x</sub> layer and the introduction of rGO which prevents the aggregation of the bimetallic nanoparticles and provides a 3D conductive network to facilitate fast charge transfer. This study demonstrates a facile yet general strategy that enables the synthesis of bimetallic systems for highly efficient electrocatalytic CO<sub>2</sub> reduction.

### 1. Introduction

Electrocatalytic reduction of CO<sub>2</sub> to value-added chemicals is a promising approach to store renewable energy in chemical bonds and produce carbon-neutral fuels.<sup>1-4</sup> However, due to the complexity of the CO<sub>2</sub> reduction reaction (CO<sub>2</sub>RR) which involves the transfer of multiple electrons and protons, developing electrocatalysts that are energy-efficient, selective, and stable presents a great challenge.<sup>5-9</sup> Various monometallic electrodes have been studied extensively as electrocatalysts for the CO<sub>2</sub>RR.<sup>10-17</sup> Depending on the nature of the surface electronic structure, each metal shows different binding energies for CO<sub>2</sub> and CO<sub>2</sub>RR intermediates, which leads to different activity and product selectivity.<sup>18,19</sup> For example, in a conventional aqueous bicarbonate solution, CO<sub>2</sub>RR on the surface of Zn, Ag and Au electrodes leads to the formation of CO while formate is the dominant product with Sn, In, Bi, and Pb electrocatalysts.<sup>20,21</sup> A range of transition metal based

molecular catalysts can also be used to reduce CO<sub>2</sub> to formate efficiently.<sup>22-24</sup>

For use in practical applications, it is necessary to develop catalysts for CO<sub>2</sub> reduction that are based on low-cost and earth-abundant elements. With this in mind, Sn is a promising electrode material due to its low cost but high selectivity towards formation of formate.<sup>25-27</sup> However, the energy efficiency of bulk Sn metal is too low for practical electrolysis, as it is reported to require at least 0.86 V of overpotential to attain a CO<sub>2</sub> reduction partial current density of 4-5 mA cm<sup>-2</sup> in an aqueous solution.<sup>28</sup> Improving the CO<sub>2</sub> reduction current density and reducing the overpotential required are critical for developing practical Sn based catalysts.

Bimetallic catalysts have attracted extensive attention in a broad range of applications in energy production and environmental remediation due to their tunable chemical/physical properties.<sup>29</sup> In changing from monometallic to bimetallic catalysts, an extra degree of freedom is introduced. Synergistic effects often arises from a binary catalyst where each chemical component on the surface of the catalyst helps to control the reactant adsorption, activation and product desorption, three necessary steps in many electrocatalytic reactions. Such a synergistic effect has been identified and employed recently to develop Sn based bimetallic catalysts with enhanced CO<sub>2</sub>RR performance.<sup>30-34</sup> Li and Sun et al.<sup>35</sup> synthesized SnO<sub>2</sub> coated Cu nanoparticles

<sup>a</sup> School of Chemistry, Monash University, Clayton 3800, Victoria, Australia.

<sup>b</sup> ARC Centre of Excellence for Electromaterials Science, Monash University, Clayton 3800, Victoria, Australia.

\*Email: jie.zhang@monash.edu

Electronic Supplementary Information (ESI) available: See DOI: 10.1039/x0xx00000x

(Cu/SnO<sub>2</sub> NPs) via thermal decomposition of tin salts in the presence of 7 nm Cu NP seeds. They found that CO<sub>2</sub> reduction on the surface of Cu/SnO<sub>2</sub> NPs is Sn-thickness dependent; the one with a thicker shell shows Sn-like activity to generate more formate whereas the one with a thinner shell is selective to the formation of CO. It is suggested that the thinner SnO<sub>2</sub> shell most likely alloys with trace Cu, causing the SnO<sub>2</sub> lattice to be uniaxially compressed and therefore favoring the production of CO over formate. Another study recently reported by Luc and Jiao et al.<sup>36</sup> reports the synthesis of Sn content controlled Ag-Sn bimetallic catalysts by galvanically displacing Sn seeds with Ag in the presence of polyvinylpyrrolidone. At 24<sub>atom</sub> % of Sn content, the highest formate faradaic efficiency (FE) of ~80% with a formate partial current density of 16 mA cm<sup>-2</sup> was observed at an applied potential of -0.8 V vs. a reversible hydrogen electrode (RHE). The catalytic activity towards formate shows a volcano-like relationship with bulk Sn content, which arises from the competing effects of favorable stabilization of OCHO\* by lattice expansion and the electron conductivity loss due to increased thickness of a surface SnO<sub>x</sub> layer. These publications demonstrate that alloying is an effective strategy for tuning the catalytic performance of Sn based catalysts.

Although improvements have been achieved, the advantages of using bimetallic catalysts for CO<sub>2</sub> reduction are still not well-explored. The primary reason lays in the difficulties presented in preparation and selection of suitable bimetallic systems. A highly efficient bimetallic catalyst requires the atomically uniform dispersion of the two metal components and a small particle size to provide sufficient catalytically active sites. Most studies to date have most conveniently been undertaken on systems where both components are completely miscible.<sup>37,38</sup> Systematic studies on bimetallic system with versatile metal-metal combinations have rarely been reported. Herein, we report the use of metal stannate derived metal-Sn bimetallic catalysts with a range of metal-Sn combinations for electrocatalytic CO<sub>2</sub> reduction. The two metal atoms in the metal stannate crystal structure are uniformly distributed in a periodic manner on the atomic scale. Electrochemical reduction of such oxides enabled the generation of well mixed alloy nanoparticles. Eight metals, Mn, Co, Ni, Cu, Zn, Ag, Pb, and Cd have been paired with Sn to form bimetallic catalysts for electrocatalytic CO<sub>2</sub> reduction in aqueous bicarbonate media.

## 2. Experimental

### 2.1 Materials and Apparatus

AgNO<sub>3</sub> (ACS reagent, 99.0%), Co(NO<sub>3</sub>)<sub>2</sub>·6H<sub>2</sub>O (ACS reagent, 99.0%), Ni(NO<sub>3</sub>)<sub>2</sub>·6H<sub>2</sub>O (97.0%), CdCl<sub>2</sub> (99.99%), Pb(NO<sub>3</sub>)<sub>2</sub> (ACS reagent, 99.0%), CuSO<sub>4</sub>·5H<sub>2</sub>O (99.0%), MnSO<sub>4</sub>·H<sub>2</sub>O (ACS reagent, 98.0%), polyvinylpyrrolidone (PVP), anhydrous SnCl<sub>4</sub> (98.0%), Nafion solution (5 wt%), and deuterium oxide (D<sub>2</sub>O, 99.9 atom % D) were purchased from Sigma-Aldrich. ZnSO<sub>4</sub>·7H<sub>2</sub>O (99.5%), NaOH (99.0%), NaHCO<sub>3</sub> (ACS grade) were purchased from Merck. All chemicals were used as supplied by the manufacturer. All aqueous solutions were prepared using

high purity water (18.2 MΩ cm) obtained from a Milli Q water purification system.

X-ray Diffraction (XRD) data were collected with a Bruker D8 ADVANCE powder diffractometer (Cu Kα radiation, λ = 0.15406 nm). Transmission electron microscopic (TEM) images were collected on a FEI Tecnai G2 T20 TWIN TEM instrument. Aberration-corrected high-angle annular dark-field scanning transmission electron microscopy (HAADF-STEM) images and energy-dispersive X-ray spectra (EDS) were acquired with a FEI Tecnai G2 F20 S-TWIN FEGTEM instrument operated at 200 kV. <sup>1</sup>H NMR experiments were undertaken with a Bruker DRX400 spectrometer using a 5 mm broadband auto-tunable probe with Z-gradients (400.1 MHz). Gas chromatography (GC) was performed with an Agilent 7820 A gas chromatography system equipped with an HP-plot molesieve (5 Å) column and a thermal conductivity detector (TCD). The carrier gas was helium (99.99%) for CO analysis while nitrogen (99.99%) was used as the carrier gas for H<sub>2</sub> analysis. The retention times were compared with those obtained with authentic samples of the gases.

### 2.2 Materials Synthesis

#### Synthesis of Na<sub>2</sub>Sn(OH)<sub>6</sub>

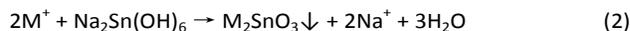
0.18 g PVP was dissolved in 10 ml of ethanol/water (4:1 in volume) mixed solution, after which 500 μL of SnCl<sub>4</sub> was added dropwise to the solution under continuous stir. After vigorous stirring for 10 min, 5 mL 12.5 M NaOH solution was added to the above solution with vigorous stirring being maintained for another 10 min. Then the mixed solution was transferred to a 20 mL Teflon lined hydrothermal autoclave and maintained at 180 °C for 24 h to enable the following reaction to occur:



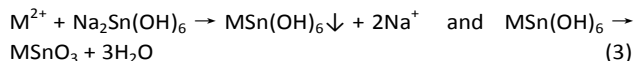
After being cooled to room temperature, the white precipitate formed in the autoclave was collected by vacuum filtration and washed with ethanol three times. Finally, the white powder was dried in vacuum at room temperature for 2 days before further use.

#### Synthesis of metal stannates

The Sn based multicomponent oxides were prepared by a cation exchange reaction between the metal ion of interest and Na<sub>2</sub>Sn(OH)<sub>6</sub> in aqueous solution according to the following reactions:



or



In detail, 5 mL of 10 mM Na<sub>2</sub>Sn(OH)<sub>6</sub> aqueous solution was added dropwise to 5 mL aqueous solution that contained 20 mM M<sup>+</sup> (Ag<sup>+</sup>) or 10 mM M<sup>2+</sup> (Cd<sup>2+</sup>, Co<sup>2+</sup>, Cu<sup>2+</sup>, Mn<sup>2+</sup>, Ni<sup>2+</sup>, Pb<sup>2+</sup>, and Zn<sup>2+</sup>) under continuous stirring. The mixed solution was stirred for a further 10 min, and then centrifuged to isolate the precipitate, which was then washed with water and ethanol

twice, and dried under vacuum at room temperature. For all the precipitates obtained from  $M^{2+}$ , further heat treatment at 350 °C (air atmosphere, 2 hours) was applied to transform  $M\text{Sn}(\text{OH})_6$  into  $M\text{SnO}_3$ .

### Synthesis of $\text{CuSnO}_3$ -graphene oxide and $\text{Ag}_2\text{SnO}_3$ -graphene oxide composites

200  $\mu\text{L}$  graphene oxide (GO) aqueous solution ( $\sim 10$  mg/mL) was added to 5 mL of 10 mM  $\text{Na}_2\text{Sn}(\text{OH})_6$  aqueous solution and ultrasonicated for 10 min. Next, the mixed solution was added dropwise to 5 mL aqueous solution that contains 20 mM  $\text{Ag}^+$  or 10 mM  $\text{Cu}^{2+}$  under continuous stirring. The mixed solution was then stirred for a further 10 min and centrifuged to isolate the precipitate. Finally, the precipitate was washed with water and ethanol twice, and dried under vacuum at room temperature.

### 2.3 Fabrication of M-Sn and M-Sn/rGO modified electrodes

To fabricate the modified electrodes, a suspension prepared from 5 mg metal stannate or metal stannate-graphene composite, 800  $\mu\text{L}$  of water, 400  $\mu\text{L}$  of ethanol, and 5  $\mu\text{L}$  of 5% Nafion solution (Sigma-Aldrich). The suspension was sonicated for 10 min to achieve a homogeneous dispersion. The resulting suspension was then coated onto a glassy carbon plate (0.3 cm  $\times$  1.4 cm) with an optimal catalyst loading of  $\sim 1$  mg  $\text{cm}^{-2}$ . The modified electrodes were then immersed in a  $\text{CO}_2$  saturated 0.5M  $\text{NaHCO}_3$  solution. A sufficiently negative potential was applied to the  $M\text{SnO}_3$  modified glassy carbon electrode to reduce  $M_x\text{SnO}_3$  to bimetallic M-Sn. For  $\text{CoSnO}_3$ ,  $\text{NiSnO}_3$ ,  $\text{CdSnO}_3$ ,  $\text{PbSnO}_3$ ,  $\text{CuSnO}_3$  and  $\text{Ag}_2\text{SnO}_3$ , a potential of -1.5 V was applied. A more negative one of -1.8 V was needed to reduce  $\text{MnSnO}_3$  and  $\text{ZnSnO}_3$ .

### 2.4 Electrochemical instrumentation and procedures

All electrochemical experiments were performed at room temperature ( $22 \pm 1$  °C) using a standard three-electrode cell configuration with a CHI700D electrochemical workstation (CHI Instruments, Austin, Texas, USA). Modified glassy carbon plate electrodes were used as the working electrodes (cathode),  $\text{Ag}/\text{AgCl}$  in 3M KCl solution as the reference electrode, and a graphite rod as the counter electrode (anode). Potentials while measured vs  $\text{Ag}/\text{AgCl}$  (3M KCl) are converted to the RHE scale using the formula:  $E(\text{vs. RHE}) = E(\text{vs. Ag}/\text{AgCl}) + 0.210 \text{ V} + 0.0586 \text{ V} \times \text{pH}$ . Bulk electrolysis was conducted in a gas tight two-compartment H-shaped electrolysis cell under a  $\text{CO}_2$  atmosphere, with a porous glass frit separating the anode and cathode compartments. High purity  $\text{CO}_2$  gas was introduced to saturate the solution and remove oxygen prior to electrochemical measurements. After bubbling with  $\text{CO}_2$  for approximately 20 min, the electrolysis cell was sealed tightly with a rubber stopper. The potentials applied during bulk electrolysis were selected based on voltammetric data obtained under the same conditions.

### 2.5 Analysis of the electrolysis products

Gas chromatography was used to identify gaseous products in

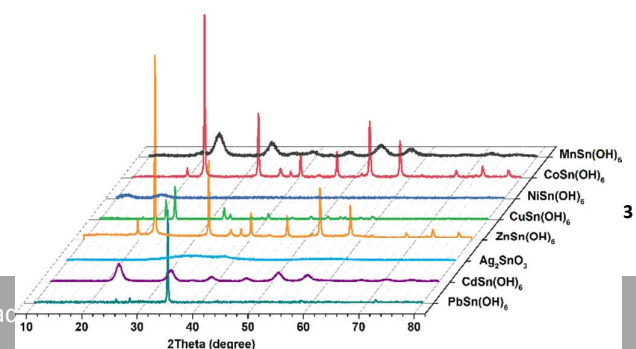
**Figure 1.** XRD patterns of  $\text{MnSn}(\text{OH})_6$  (black trace),  $\text{CoSn}(\text{OH})_6$  (red trace),  $\text{NiSn}(\text{OH})_6$  (blue trace),  $\text{CuSn}(\text{OH})_6$  (green trace),  $\text{ZnSn}(\text{OH})_6$  (orange trace),  $\text{Ag}_2\text{SnO}_3$  (cyan trace),  $\text{CdSn}(\text{OH})_6$  (purple trace), and  $\text{PbSn}(\text{OH})_6$  (dark cyan trace).

the headspace. Calibration curves for  $\text{H}_2$  and  $\text{CO}$  were constructed by injecting known amounts of pure  $\text{H}_2$  and  $\text{CO}$  and plotting the peak area against the amount injected. The gaseous products were identified by comparing the retention times with pure standard gases and quantified from the relevant calibration curves. The liquid product(s) was analysed by  $^1\text{H}$  NMR spectroscopy. In these NMR analyses, normally, 500  $\mu\text{L}$  of electrolysed solution was mixed with 100  $\mu\text{L}$   $\text{D}_2\text{O}$  and 100  $\mu\text{L}$   $\text{DMSO}/\text{H}_2\text{O}$  (1/1000 by volume), where  $\text{D}_2\text{O}$  was used as a deuterated source and  $\text{DMSO}$  was used as an internal standard.

## 3. Results and discussion

### 3.1 Structure and morphology of metal stannates

Metal stannates represent an important class of functional ternary oxide materials often having unique optical, electronic, and magnetic properties.<sup>39</sup> Classes of stannates include perovskite-type metal hydroxystannates ( $M_x\text{Sn}(\text{OH})_6$ ,  $x = 2$  for a monocation and 1 for a dication), metal stannates ( $M_x\text{SnO}_3$ ), often described as metal oxide solid solutions ( $M_x\text{O}-\text{SnO}_2$ ), and spinel type di-metal stannates ( $M_{2x}\text{SnO}_4$ ). The co-existence of two different metal ions within ternary metal oxides demands strict stoichiometry control during synthesis. In this work, a facile cation exchange reaction in aqueous solution under ambient conditions was adopted to synthesize perovskite-type metal hydroxystannates, as described in the Experimental Section. Eight metal ions,  $\text{Mn}^{2+}$ ,  $\text{Co}^{2+}$ ,  $\text{Ni}^{2+}$ ,  $\text{Cu}^{2+}$ ,  $\text{Zn}^{2+}$ ,  $\text{Ag}^+$ ,  $\text{Cd}^{2+}$  and  $\text{Pb}^{2+}$  have been used to replace sodium ions in  $\text{Na}_2\text{Sn}(\text{OH})_6$  in order to form metal hydroxystannates. Figure 1 shows the XRD powder patterns derived from the as-obtained metal hydroxystannates. For  $\text{Mn}^{2+}$ ,  $\text{Co}^{2+}$ ,  $\text{Cu}^{2+}$ ,  $\text{Zn}^{2+}$ ,  $\text{Cd}^{2+}$  and  $\text{Pb}^{2+}$  derived hydroxystannates, the XRD pattern matches the standard JCPDS cards of  $\text{MnSn}(\text{OH})_6$  (89-7359),  $\text{CoSn}(\text{OH})_6$  (13-356),  $\text{CuSn}(\text{OH})_6$  (70-117),  $\text{ZnSn}(\text{OH})_6$  (74-1825),  $\text{CdSn}(\text{OH})_6$  (28-202), and  $\text{PbSn}(\text{OH})_6$  (73-986), respectively. For the  $\text{Ni}^{2+}$  derived product, no strong characteristic diffraction peaks were found, due to the low crystallinity of the as-obtained  $\text{NiSn}(\text{OH})_6$  with ultra-fine particle size.  $\text{Ag}^+$  is a much stronger Lewis acid than the other metals used here; hence, the  $\text{Ag}^+$  derived product is in the form of a stannate ( $\text{Ag}_2\text{SnO}_3$ ) instead of a hydroxystannate. The XRD powder pattern of  $\text{Ag}_2\text{SnO}_3$  is very broad and matches that expected for highly amorphous  $\text{Ag}_2\text{SnO}_3$  reported in literature,<sup>40</sup> which is more like a solid solution of  $\text{Ag}_2\text{O}$  and  $\text{SnO}_2$ .



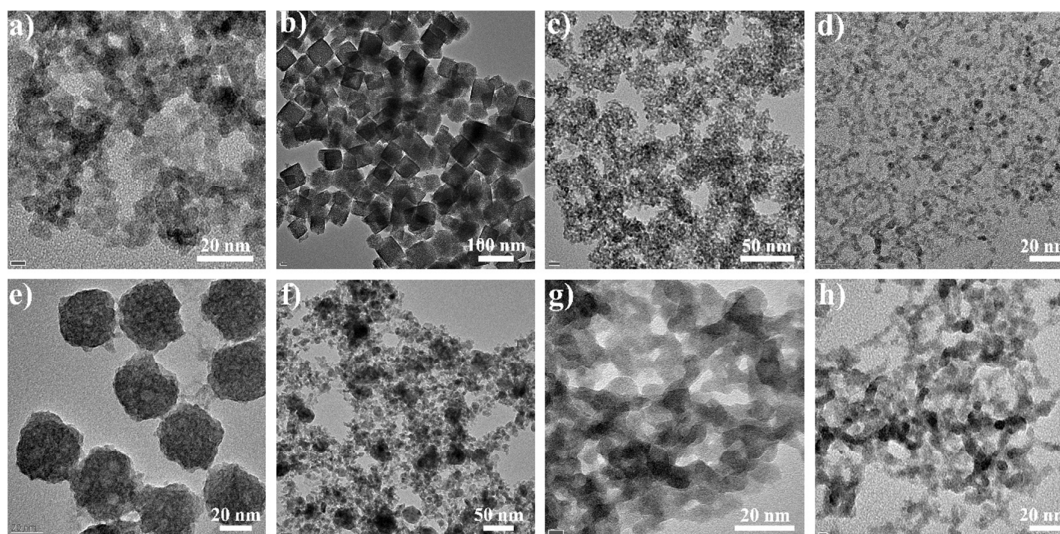


Figure 2. TEM images of MnSnO<sub>3</sub> (a), CoSnO<sub>3</sub> (b), NiSnO<sub>3</sub> (c), CuSnO<sub>3</sub> (d), ZnSnO<sub>3</sub> (e), Ag<sub>2</sub>SnO<sub>3</sub> (f), CdSnO<sub>3</sub> (g), PbSnO<sub>3</sub> (h).

The metal hydroxystannates were subsequently annealed at 350 °C in air for 1 hour to remove the crystalline water and transform into metal stannates. After annealing, all the characteristic diffraction peaks of the metal hydroxystannates were absent. Instead, broad diffraction patterns with low-intensity features were obtained (Figure S1), indicating the formation of highly amorphous metal stannates (MSnO<sub>3</sub>). The morphologies of all the MSnO<sub>3</sub> samples were characterized by TEM, as shown in Figure 2. All samples are composed of fine nanoparticles having a size below 50 nm. Specifically, MnSnO<sub>3</sub> (Figure 2a) is composed of uniform nanoparticles with an average particle size of 6.4 nm. CoSnO<sub>3</sub> (Figure 2b) has an interesting porous nano-cube structure, with an average size of 43 nm. NiSnO<sub>3</sub> (Figure 2c) shows an ultra-small particle size of 3.5 nm. CuSnO<sub>3</sub> (Figure 2d) also has a small average particle size of 3.8 nm. ZnSnO<sub>3</sub> (Figure 2e) shows a porous nano-sphere structure with an average size of 36 nm. Ag<sub>2</sub>SnO<sub>3</sub> (Figure 2f) has a less uniform particles size distribution; most of the nanoparticles have a size located around 6.6 nm, while some larger aggregates with an average size of 23 nm also are found. CdSnO<sub>3</sub> (Figure 2g) and PbSnO<sub>3</sub> (Figure 2h) are composed of uniform nanoparticles with a size of 8.1 nm and 5.6 nm, respectively. It should be mentioned that, in the case of Ag<sub>2</sub>SnO<sub>3</sub>, high resolution TEM revealed that the small particles contain a crystal lattice which is assigned to (110) plane of SnO<sub>2</sub>, while (200) planes of Ag<sub>2</sub>O are found on the large particles. This is due to Ag<sub>2</sub>SnO<sub>3</sub> being light sensitive and decomposing to form a mixed system of Ag<sub>2</sub>O-SnO<sub>2</sub>.

### 3.2 Metal stannate derived bimetallic catalysts for CO<sub>2</sub> reduction

Phase identification of the reduced metal stannates was carried out by XRD. Figures S2 to S9 show the XRD patterns derived from the eight metal-Sn materials and their

corresponding JCPDS standard cards. Zn-Sn, Cd-Sn, and Pb-Sn consist of separated metallic Zn, Cd, Pb, and Sn. The other five materials form or partially form metal-Sn alloys. In summary, Mn-Sn contains MnSn<sub>2</sub> alloy and Sn; Co-Sn contains only CoSn alloy; Ni-Sn contains Ni<sub>3</sub>Sn alloy and Sn; Cu-Sn contains CuSn alloy; Ag-Sn contains Ag<sub>3</sub>Sn alloy and Sn.

After the reduction process, the M-Sn bimetallic material modified glassy carbon electrode was immediately transferred to a gas-tight H type cell filled with CO<sub>2</sub> saturated 0.5M NaHCO<sub>3</sub> solution in order to perform bulk electrolysis experiments. For a rapid assessment of the CO<sub>2</sub> reduction performance of the metal stannate derived bimetallic materials, constant potential electrolysis was conducted at -1.5 V, which is located within the potential range that most Sn based metallic catalysts showed high selectivity towards formate.<sup>26, 36, 41</sup> Figure 3a shows the FE values of the eight M-Sn bimetallic catalysts. For Co-Sn, Ni-Sn, and Mn-Sn, hydrogen was the dominant product with correspondingly high FEs of 99%, 94%, and 93%, respectively. CO was only detected for the Cd-Sn, Pb-Sn, Zn-Sn, Cu-Sn, and Ag-Sn catalysts, where the highest FE<sub>CO</sub> of 24% was obtained with PbSn. The FE for formate on these five bimetallic catalysts reached 47%, 59%, 50%, 76%, and 80%, respectively. Cu-Sn and Ag-Sn showed the highest selectivity towards the formation of formate. The product selectivity is rationalized by the composition of the

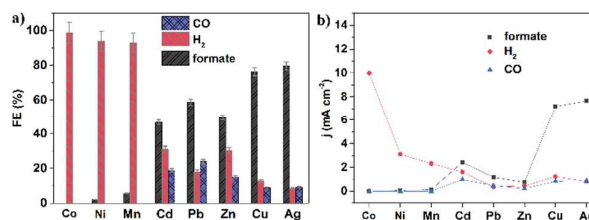


Figure 3. a) Faradaic efficiency and b) partial current values of M-Sn (M = Co, Ni, Mn, Cd, Pb, Zn, Cu, Ag) bimetallic catalysts for CO<sub>2</sub> reduction in 0.5M NaHCO<sub>3</sub> media at -1.5 V vs. Ag/AgCl.

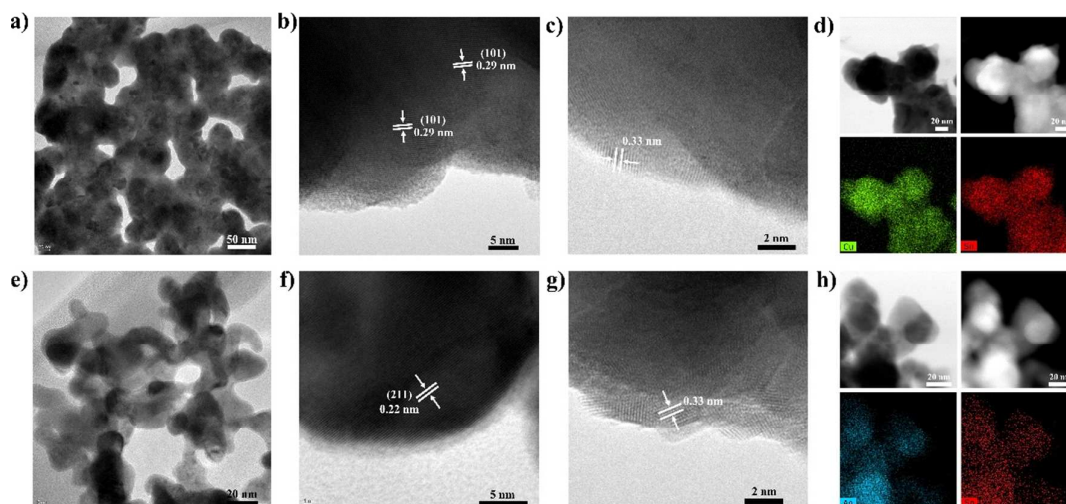


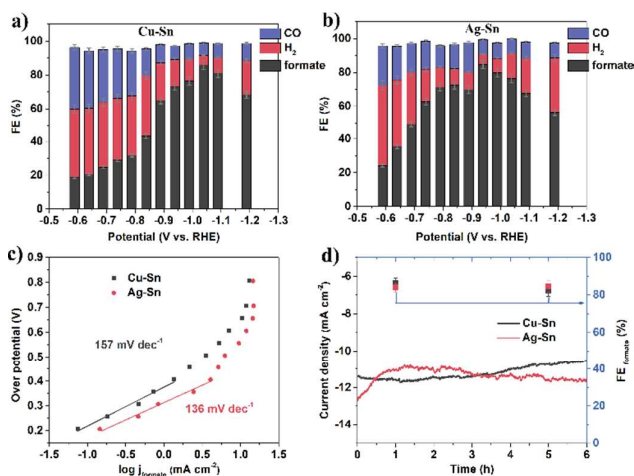
Figure 4. TEM, HRTEM, STEM-HAADF plus EDS mapping images of Cu-Sn (a,b,c,d) and Ag-Sn (e,f,g,h) bimetallic catalyst.

bimetallic catalysts. The Co-Sn, Mn-Sn, and Ni-Sn catalysts tend to form a Sn@M structure, as Co, Mn, and Ni are harder to be reduced than Sn. Since Co, Mn, and Ni are also highly active HER catalysts in aqueous solution, the Co-Sn, Mn-Sn, and Ni-Sn catalysts produced mainly  $\text{H}_2$ . In the case of Cu-Sn and Ag-Sn, they are more likely to form a M@Sn structure, and hence provided a performance that resemble the Sn component, as discussed below. Zn-Sn, Cd-Sn, and Pb-Sn form separate metallic Zn, Cd, Pb, and Sn. As a result, they exhibited performance that is intermediate to that for the M and the Sn component. Besides product selectivity, the partial current density for the  $\text{CO}_2\text{RR}$  is another important criterion for defining a good catalyst. This parameter indicates the facileness of the catalytic process. In this context, Cd-Sn, Pb-Sn, and Zn-Sn are not considered to be good  $\text{CO}_2$  reduction catalysts on the basis of their cyclic voltammograms (Figure S10), even if the current derived entirely from  $\text{CO}_2$  reduction. Figure 3b presents the partial current distribution of the bimetallic catalysts at  $-1.5$  V. Compared with the other bimetallic catalysts, Cu-Sn and Ag-Sn exhibited significantly larger partial current densities for the formation of formate, reaching  $7.2 \text{ mA cm}^{-2}$  and  $7.6 \text{ mA cm}^{-2}$  respectively. Both Cu-Sn and Ag-Sn showed improved performance relative to that of Sn metal,<sup>25, 42</sup> which encouraged us to further evaluate the  $\text{CO}_2\text{RR}$  performance of the more efficient Cu-Sn and Ag-Sn bimetallic systems.

### 3.3 $\text{CO}_2$ reduction on stannate derived Cu-Sn and Ag-Sn bimetallic catalysts

The TEM image (Figure 4a) of the Cu-Sn bimetallic catalyst shows an aggregated nanoparticulate morphology with an average size of 60 nm. The HRTEM image (Figure 4b) revealed the existence of crystal lattices with d-spacing of 0.29 nm, which is in accordance with the value expected for the (101) plane of a CuSn alloy. These results, in tandem with the XRD

powder pattern, proved that the Cu-Sn bimetallic catalyst existed in the form of a CuSn alloy, well-known as bronze. This CuSn alloy possesses a hexagonal crystal structure, where Cu and Sn atoms are dispersed in a periodic manner.<sup>43</sup> Each Cu atom is surrounded by 6 Sn atoms, and each Sn atom is also surrounded by 6 Cu atoms.  $\text{SnO}_2$  nanocrystals were found on the surface of the CuSn alloy nanoparticles (Figure 4c), although theoretically, the transformation of  $\text{CuSnO}_3$  to the CuSn alloy should lead to a stoichiometric product. Since CuO can be more easily reduced than  $\text{SnO}_2$ , residual  $\text{SnO}_x$  covering the Cu alloy could be present even when a very negative potential is applied. From EDS mapping results obtained from STEM-HAADF (Figure 4d), both Cu and Sn elements are uniformly dispersed within the nanoparticles. Selected area diffraction (SAD) pattern (Figure S11a) of the Cu-Sn nanoparticles reveal typical polycrystalline character. The 5 main diffraction rings possess interplanar distances of 0.29, 0.25, 0.21, 0.17, and 0.12 nm, corresponding to the (101), (002), (110), (201), and (212) planes of the CuSn alloy, respectively. Similarly, the Ag-Sn bimetallic catalyst has an interconnected nano particulate morphology with an average size of 21 nm (Figure 4e). Crystal lattices with d-spacing of 0.22 nm were found in the HRTEM image (Figure 4f), which is in accordance with the interplanar distance of the (211) plane of  $\text{Ag}_3\text{Sn}$  alloy. Stoichiometrically, the ratio of Ag and Sn atoms in  $\text{Ag}_3\text{Sn}$  alloy is 3:1, which is higher than that of the precursor  $\text{Ag}_2\text{SnO}_3$ , implying co-existence of another form of Sn. However, judging from EDS mapping results obtained from STEM-HAADF (Figure 4h), both Ag and Sn elements are uniformly dispersed over the entire sample and no individual Sn or  $\text{SnO}_x$  particles were found. Instead, the Ag-Sn catalysts is covered by a thin layer having a thickness of  $\sim 2$  nm (Figure 4g). Within this thin layer, an ordered interplanar structure with a d-spacing of 0.33 nm was found, which is in accordance with the d-spacing value of the (110) plane of  $\text{SnO}_2$ . The excess surface Sn content is derived from the residual Sn released



during the transformation of  $\text{Ag}_2\text{SnO}_3$  to  $\text{Ag}_3\text{Sn}$ . The existence of the  $\text{SnO}_2$  layer implies the formation of a metastable  $\text{SnO}_x$  layer on the catalyst under  $\text{CO}_2$  reduction conditions, which can act as the catalytically active sites for  $\text{CO}_2$  reduction.<sup>19</sup> In the meantime, the  $\text{Ag}_3\text{Sn}$  nanoparticles can act as a conductive framework to support the  $\text{SnO}_x$  thin layer, enabling fast electron transportation. Selected area diffraction patterns

**Figure 5.**  $\text{CO}$ ,  $\text{H}_2$ , and formate faradaic efficiency as a function of potential for Cu-Sn (a) and Ag-Sn bimetallic catalysts. (c) Tafel analysis, and (d) i-t curves of bulk electrolysis on Cu-Sn and Ag-Sn bimetallic catalyst in bicarbonate media.

(Figure S11b) of the Ag-Sn nanoparticles reveal typical polycrystalline characteristics. The 7 main diffractions rings possess interplanar distances of 0.26, 0.24, 0.22, 0.17, 0.15, 0.14, and 0.13 nm, corresponding to the (201), (020), (211), (022), (203), (032), and (223) planes of  $\text{Ag}_3\text{Sn}$  alloy, respectively.

A series of controlled potential bulk electrolysis experiments were carried out to comprehensively establish the electrocatalytic  $\text{CO}_2$  reduction performance of both Cu-Sn and Ag-Sn catalysts. The FE values for the products with Cu-Sn and Ag-Sn catalysts are presented as a function of applied potential from -0.59 V to -1.19 V (vs. RHE) in Figures 5a&b, which shows that  $\text{CO}$ ,  $\text{H}_2$ , and formate are the main products with a combined FE close to 100% over the whole potential range. No other products were detected by NMR or GC. The FE values for each product are dependent on the applied potential. For both Cu-Sn and Ag-Sn,  $\text{CO}$  and  $\text{H}_2$  have higher FEs at more positive potentials, whereas the FE for formate increase rapidly with increasingly negative potential. At -0.59 V vs. RHE, the FE for formate on Ag-Sn (24%) is slightly higher than that of Cu-Sn (19%). For Ag-Sn, the FE for formate ( $\text{FE}_{\text{formate}}$ ) reaches a maximum of 85% at -0.94 V vs. RHE (corresponding to an overpotential of 0.85 V for formate), after which it decreases as the potential is made more negative. In contrast, the  $\text{FE}_{\text{formate}}$  on Cu-Sn reaches a maximum value of 86% at -1.04 V vs. RHE. Figure S12 shows the partial current densities of the products as a function of applied potential. For Ag-Sn, the partial current density of formate starts to increase

dramatically at -0.69 V vs. RHE, reaching  $9.6 \text{ mA cm}^{-2}$  at -0.94 V vs. RHE and  $14.8 \text{ mA cm}^{-2}$  at -1.09 V vs. RHE. For Cu-Sn, a rapid increase in partial current density of formate started from -0.79 V vs. RHE, reaching  $10.4 \text{ mA cm}^{-2}$  at -1.04 V vs. RHE and  $13.0 \text{ mA cm}^{-2}$  at -1.19 V vs. RHE. In both cases, the partial current density for  $\text{CO}$  does not vary significantly with potential, while that of  $\text{H}_2$  starts to increase rapidly when the potential is more negative than -1 V vs. RHE. The formate partial current density at various overpotentials were calculated. Tafel analysis was undertaken using the data obtained from the lower overpotential region where the contribution from mass transport is insignificant (Figure 5c). Tafel slopes of  $157 \text{ mV dec}^{-1}$  and  $136 \text{ mV dec}^{-1}$  were obtained for the Cu-Sn and Ag-Sn catalysts, respectively, suggesting that the first electron transfer process is the rate determining step.<sup>29</sup> Figure 5d presents the i-t curves for 6 h bulk electrolysis experiments for Cu-Sn and Ag-Sn at -1.04 V and -0.94 V vs. RHE, respectively. In both cases, a stable current density of  $\sim 11 \text{ mA cm}^{-2}$  was maintained for the duration.

### 3.4 Incorporating Cu-Sn and Ag-Sn bimetallic catalysts with rGO

Compared with other Sn based formate-selective  $\text{CO}_2$  reduction catalysts reported in the literature (Table S1), the Cu-Sn and Ag-Sn bimetallic catalysts have a lower potential requirement to reach the maximum selectivity for formate formation. However, the current density obtained is a factor of 4 smaller than reported in the literature,<sup>26, 44</sup> due to use of 2D (glassy carbon plate) rather than 3D (carbon paper) electrodes. To enhance the current density, reduced graphene oxide (rGO) was integrated with the Cu-Sn and Ag-Sn bimetallic systems to provide a 3D conductive network.  $\text{CuSnO}_3$ -GO and  $\text{Ag}_2\text{SnO}_3$ -GO composites were first synthesized as described in the Experimental Section. TEM images of these two composites are presented in the Supporting Information (Figure S13). Cu-Sn/rGO and Ag-Sn/rGO were obtained by the electrochemical reduction of  $\text{CuSnO}_3$ -GO and  $\text{Ag}_2\text{SnO}_3$ -GO composites. The introduction of rGO in these bimetallic systems achieved a uniform distribution of the nanoparticles during electrolysis, as shown in TEM images (Figure 6a,d). HRTEM images reveal the (110) plane of CuSn alloy with a d-spacing of 0.21 nm (Figure 6b) and the (211) plane of  $\text{Ag}_3\text{Sn}$  alloy with a d-spacing of 0.22 nm (Figure 6e). XRD pattern also proved that Cu-Sn (Figure 6c) is still composed of CuSn alloy and Ag-Sn (Figure 6f) of  $\text{Ag}_3\text{Sn}$  alloy along with metallic Sn in these nanocomposites.

The rGO incorporated bimetallic systems are capable of providing more catalytic active sites on the electrode surface,

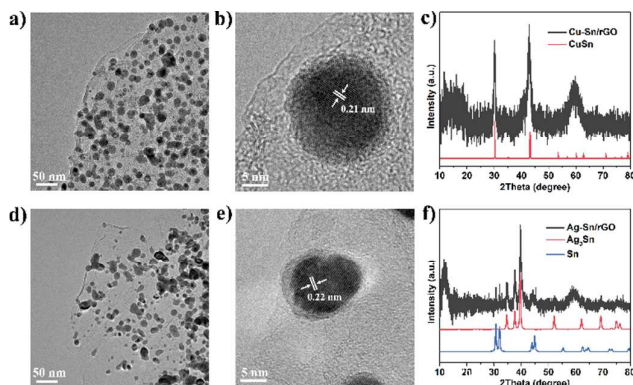
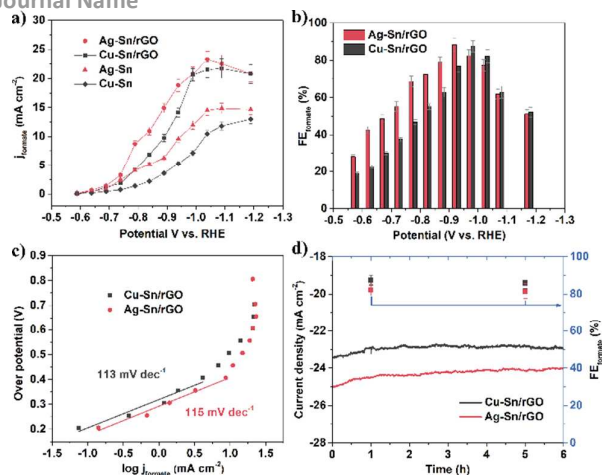


**Figure 6.** TEM, HRTEM images and XRD patterns of Cu-Sn/rGO (a,b,c) and Ag-Sn/rGO (d,e,f).



which leads to significantly improved catalytic current density. Figure 7a shows the formate partial current density as a function of potential for Cu-Sn and Ag-Sn with and without the presence of rGO. At  $-0.99$  V vs. RHE, the presence of rGO helped increase the formate partial current density from  $7.1$

**Figure 7.** a) Formate partial current density as a function of potential for Cu-Sn/rGO, Ag-Sn/rGO, Cu-Sn, and Ag-Sn. Formate faradaic efficient plotted as a function of potential (b), Tafel analysis (c), and i-t curves of bulk electrolysis (d) on Cu-Sn/rGO and Ag-Sn/rGO bimetallic catalyst in bicarbonate media.

$\text{mA cm}^{-2}$  to  $20.6 \text{ mA cm}^{-2}$  for Cu-Sn, and  $12 \text{ mA cm}^{-2}$  to  $20.7 \text{ mA cm}^{-2}$  for Ag-Sn. Furthermore, the addition of rGO also slightly improved the selectivity for formate, as shown in Figure 7b. Ag-Sn/rGO reaches the highest  $\text{FE}_{\text{formate}}$  of 88.3% at  $-0.94$  V vs. RHE, while Cu-Sn/rGO has its highest  $\text{FE}_{\text{formate}}$  of 87.4% at  $-0.99$  V vs. RHE. Both Ag-Sn/rGO and Cu-Sn/rGO show lower Tafel slopes of  $115 \text{ mV dec}^{-1}$  and  $113 \text{ mV dec}^{-1}$ , respectively, which indicates that the first electron transfer process is still the rate determining step.<sup>42, 45, 46</sup> These values are close to the Tafel slope obtained for  $\text{Ag}_{76}\text{Sn}_{24}$  with a core-shell structure.<sup>36</sup> The stability of the two rGO composite catalysts were monitored during long term bulk electrolysis experiments at  $-0.99$  V vs. RHE. Figure 7d shows the corresponding i-t data for 6 hours along with  $\text{FE}_{\text{formate}}$  values at the first and the fifth hour. Both Cu-Sn/rGO and Ag-Sn/rGO exhibited a stable catalytic current for the entire time-scale, with  $\text{FE}_{\text{formate}}$  variation of below 2%. TEM images of Cu-Sn/rGO (a,b) and Ag-Sn/rGO (c,d) taken after electrolysis (Figure S14) show no obvious morphology change, confirming the high structural stability of the catalysts. Compared with other Sn based formate selective catalysts (Table S1), both Cu-Sn/rGO and Ag-Sn/rGO show the advantage of low overpotential, high selectivity towards formate, together with high catalytic current density. The significantly improved performance of these type of bimetallic nanoparticle/rGO composite catalysts are attributed to the small particle size of the stannate derived bimetallic nanoparticles, the  $\text{SnO}_x$  layer formed on the surface of the bimetallic nanoparticles and the introduction of rGO which prevents the aggregation of the bimetallic nanoparticles and provides a 3D conductive network to facilitate fast charge transfer.

## Conclusions

In summary, 8 metal-Sn (metal = Mn, Co, Ni, Cu, Zn, Ag, Cd, and Pb) bimetallic nanoparticles have been synthesized by electrochemical reduction of metal stannates and assessed as electrocatalysts for electrochemical  $\text{CO}_2$  reduction. Zn-Sn, Cd-Sn, and Pb-Sn form separated metallic Zn, Cd, Pb, and Sn, while the other five materials form or partially form metal-Sn alloys. Among all the composites examined, the Ag-Sn and Cu-Sn bimetallic systems showed the highest selectivity and activity for formate formation. When incorporated with rGO, the Ag-Sn/rGO catalyst reaches its highest  $\text{FE}_{\text{formate}}$  of 88.3% at  $-0.94$  V vs. RHE with a current density of  $21.3 \text{ mA cm}^{-2}$ , while the Cu-Sn/rGO catalyst has its highest  $\text{FE}_{\text{formate}}$  of 87.4% at  $-0.99$  V vs. RHE with a current density of  $23.6 \text{ mA cm}^{-2}$ , making them among the best performed  $\text{CO}_2$  reduction Sn catalysts reported so far. Thus, a combination of these electrocatalytic  $\text{CO}_2$  reduction systems with a  $\text{CO}_2$  capture/concentration process may provide a feasible route for commercial application. This work demonstrates a facile yet general strategy that enables the synthesis of bimetallic systems that in some cases achieved highly efficient electrocatalytic  $\text{CO}_2$  reduction. The main drawback of this strategy is that it is not possible to adjust the ratio of the two metal components. Nevertheless, this type of strategy should apply to other ternary oxide systems and allow fast screening of high performance bimetallic catalysts to be achieved for  $\text{CO}_2$  reduction and other reactions.

## Conflicts of interest

There are no conflicts to declare.

## Acknowledgements

The authors acknowledge the use of facilities provided by the Monash Centre for Electron Microscopy and the Monash X-Ray Platform.

## References

1. Z. W. Seh, J. Kibsgaard, C. F. Dickens, I. Chorkendorff, J. K. Nørskov and T. F. Jaramillo, *Science*, 2017, **355**, 146.
2. C. W. Li, J. Ciston and M. W. Kanan, *Nature*, 2014, **508**, 504-507.
3. M. Alvarez-Guerra, J. Albo, E. Alvarez-Guerra and A. Irabien, *Energy & Environmental Science*, 2015, **8**, 2574-2599.
4. E. V. Kondratenko, G. Mul, J. Baltrusaitis, G. O. Larrazabal and J. Perez-Ramirez, *Energy & Environmental Science*, 2013, **6**, 3112-3135.
5. Y. Li and Q. Sun, *Advanced Energy Materials*, 2016, **6**, 1600463.
6. J. Albo, M. Alvarez-Guerra, P. Castano and A. Irabien, *Green Chemistry*, 2015, **17**, 2304-2324.

7. A. M. Appel, J. E. Bercaw, A. B. Bocarsly, H. Dobbek, D. L. DuBois, M. Dupuis, J. G. Ferry, E. Fujita, R. Hille, P. J. A. Kenis, C. A. Kerfeld, R. H. Morris, C. H. F. Peden, A. R. Portis, S. W. Ragsdale, T. B. Rauchfuss, J. N. H. Reek, L. C. Seefeldt, R. K. Thauer and G. L. Waldrop, *Chemical Reviews*, 2013, **113**, 6621-6658.
8. F. Urbain, P. Tang, N. M. Carretero, T. Andreu, L. G. Gerling, C. Voz, J. Arbiol and J. R. Morante, *Energy & Environmental Science*, 2017, **10**, 2256-2266.
9. Y. Yang, S. Ajmal, X. Zheng and L. Zhang, *Sustainable Energy & Fuels*, 2018, **2**, 510-537.
10. Y. Hori, *Electrochemical CO<sub>2</sub> reduction on metal electrode*, Springer, New York, 2008.
11. M. R. Singh, Y. Kwon, Y. Lum, J. W. Ager and A. T. Bell, *Journal of the American Chemical Society*, 2016, **138**, 13006-13012.
12. K. P. Kuhl, E. R. Cave, D. N. Abram and T. F. Jaramillo, *Energy & Environmental Science*, 2012, **5**, 7050-7059.
13. J. H. Koh, D. H. Won, T. Eom, N.-K. Kim, K. D. Jung, H. Kim, Y. J. Hwang and B. K. Min, *ACS Catalysis*, 2017, **7**, 5071-5077.
14. S. Gao, Y. Lin, X. Jiao, Y. Sun, Q. Luo, W. Zhang, D. Li, J. Yang and Y. Xie, *Nature*, 2016, **529**, 68-71.
15. C. Rogers, W. S. Perkins, G. Veber, T. E. Williams, R. R. Cloke and F. R. Fischer, *J Am Chem Soc*, 2017, **139**, 4052-4061.
16. C. Ding, A. Li, S.-M. Lu, H. Zhang and C. Li, *ACS Catalysis*, 2016, **6**, 6438-6443.
17. S. Zhang, P. Kang and T. J. Meyer, *Journal of the American Chemical Society*, 2014, **136**, 1734-1737.
18. X. Liu, J. Xiao, H. Peng, X. Hong, K. Chan and J. K. Nørskov, *Nature Communications*, 2017, **8**, 15438.
19. J. T. Feaster, C. Shi, E. R. Cave, T. Hatsukade, D. N. Abram, K. P. Kuhl, C. Hahn, J. K. Nørskov and T. F. Jaramillo, *ACS Catalysis*, 2017, **7**, 4822-4827.
20. J. Qiao, Y. Liu, F. Hong and J. Zhang, *Chemical Society Reviews*, 2014, **43**, 631-675.
21. F. Quan, D. Zhong, H. Song, F. Jia and L. Zhang, *Journal of Materials Chemistry A*, 2015, **3**, 16409-16413.
22. A. Taheri, E. J. Thompson, J. C. Fettinger and L. A. Berben, *ACS Catalysis*, 2015, **5**, 7140-7151.
23. S. Roy, B. Sharma, J. Pécaut, P. Simon, M. Fontecave, P. D. Tran, E. Derat and V. Artero, *Journal of the American Chemical Society*, 2017, **139**, 3685-3696.
24. P. Kang, C. Cheng, Z. Chen, C. K. Schauer, T. J. Meyer and M. Brookhart, *Journal of the American Chemical Society*, 2012, **134**, 5500-5503.
25. Y. Chen and M. W. Kanan, *Journal of the American Chemical Society*, 2012, **134**, 1986-1989.
26. F. Li, L. Chen, G. P. Knowles, D. R. MacFarlane and J. Zhang, *Angew Chem Int Ed Engl*, 2017, **56**, 505-509.
27. E. Irtem, T. Andreu, A. Parra, M. D. Hernandez-Alonso, S. Garcia-Rodriguez, J. M. Riesco-Garcia, G. Penelas-Perez and J. R. Morante, *Journal of Materials Chemistry A*, 2016, **4**, 13582-13588.
28. Y. Hori, H. Wakebe, T. Tsukamoto and O. Koga, *Electrochimica Acta*, 1994, **39**, 1833-1839.
29. S. De, J. Zhang, R. Luque and N. Yan, *Energy & Environmental Science*, 2016, **9**, 3314-3347.
30. S. Sarfraz, A. T. Garcia-Esparza, A. Jedidi, L. Cavallo and K. Takanebe, *ACS Catalysis*, 2016, **6**, 2842-2851.
31. G. Yin, H. Abe, R. Kodiyath, S. Ueda, N. Srinivasan, A. Yamaguchi and M. Miyauchi, *Journal of Materials Chemistry A*, 2017, **5**, 12113-12119.
32. E. L. Clark, C. Hahn, T. F. Jaramillo and A. T. Bell, *J Am Chem Soc*, 2017, **139**, 15848-15857.
33. S. Rasul, D. H. Anjum, A. Jedidi, Y. Minenkov, L. Cavallo and K. Takanebe, *Angewandte Chemie-International Edition*, 2015, **54**, 2146-2150.
34. A. Jedidi, S. Rasul, D. Masih, L. Cavallo and K. Takanebe, *Journal of Materials Chemistry A*, 2015, **3**, 19085-19092.
35. Q. Li, J. Fu, W. Zhu, Z. Chen, B. Shen, L. Wu, Z. Xi, T. Wang, G. Lu, J. J. Zhu and S. Sun, *J Am Chem Soc*, 2017, **139**, 4290-4293.
36. W. Luc, C. Collins, S. Wang, H. Xin, K. He, Y. Kang and F. Jiao, *Journal of the American Chemical Society*, 2017, **139**, 1885-1893.
37. W. Yu, M. D. Porosoff and J. G. Chen, *Chemical Reviews*, 2012, **112**, 5780-5817.
38. M. Sankar, N. Dimitratos, P. J. Miedziak, P. P. Wells, C. J. Kiely and G. J. Hutchings, *Chemical Society Reviews*, 2012, **41**, 8099-8139.
39. C. Liu, H. Chen, Z. Ren, S. Dardona, M. Piech, H. Gao and P.-X. Gao, *Applied Surface Science*, 2014, **296**, 53-60.
40. K. Yin, F. Liao, Y. Zhu, A. Gao, T. Wang and M. Shao, *Journal of Materials Chemistry C*, 2014, **2**, 10082-10086.
41. Y. Li, J. Qiao, X. Zhang, T. Lei, A. Girma, Y. Liu and J. Zhang, *ChemElectroChem*, 2016, **3**, 1618-1628.
42. J. J. Wu, F. G. Risalvato, S. G. Ma and X. D. Zhou, *Journal of Materials Chemistry A*, 2014, **2**, 1647-1651.
43. S. Fürtauer, D. Li, D. Cupid and H. Flandorfer, *Intermetallics*, 2013, **34**, 142-147.
44. S. Y. Choi, S. K. Jeong, H. J. Kim, I. H. Baek and K. T. Park, *Acs Sustainable Chemistry & Engineering*, 2016, **4**, 1311-1318.
45. M. F. Baruch, J. E. Pander, J. L. White and A. B. Bocarsly, *Acs Catalysis*, 2015, **5**, 3148-3156.
46. E. Gileadi, *Electrode kinetics for chemists, engineers, and materials scientists*, Wiley-VCH, Weinheim, 1993.